

Investigations of electric monopole transitions in medium-mass to heavy nuclei: Beyond mean field calculations with the Gogny force

J.-P. Delaroche,^{1,2} J. Libert,¹ M. Girod,^{1,2} I. Deloncle,^{3,1} and M. Dupuis^{1,2,*}

¹CEA, DAM, DIF F-91297 Arpajon, France

²Université Paris-Saclay, CEA, Laboratoire Matière en Conditions Extrêmes, F-91680 Bruyères-le-Châtel, France

³Université Paris-Saclay, CNRS/IN2P3, IJCLab 91405 Orsay, France



(Received 31 March 2023; accepted 24 October 2023; published 17 January 2024)

The five dimensional collective Hamiltonian (5DCH) implemented with Gogny force has been employed in systematic calculations of electric monopole ($E0$) transitions in even-even nuclei with masses $30 < A < 310$. Significant improvements in the comparison between experimental data and calculations are achieved using (i) stronger collective masses than those inferred from the Inglis-Beliaev approximation and (ii) the $E0$ transition operator as defined by Church and Weneser [E. L. Church and J. Weneser, *Phys. Rev.* **103**, 1035 (1956)]. Main emphasis has been placed on the square of the $E0$ transition strength, $\rho^2(E0; 0_2^+ \rightarrow 0_1^+)$, for transitions between the first 0^+ excited state and ground state levels. The dimensionless parameter $X(E0/E2)$ has also been considered in 5DCH calculations covering the rare earth and actinide regions where sparse data are available. Finally, the quasiparticle random-phase approximation (QRPA) implemented with Gogny force has been considered as a complementary model for the interpretation of $\rho^2(E0; 0_i^+ \rightarrow 0_1^+)$, $i \neq 2$, data available for ^{166}Er and ^{238}U . The 5DCH model provides a reasonable description of collective $E0$ transitions, but fails otherwise. Specific shell effects are not considered in the present modeling. Global improvements in $\rho^2(E0)$ and $X(E0/E2)$ predictions would be achieved by implementing the energy density functional with quasiparticle components.

DOI: [10.1103/PhysRevC.109.014320](https://doi.org/10.1103/PhysRevC.109.014320)

I. INTRODUCTION

The nature of the first excited 0^+ state of even-even nuclei spread over the periodic table has remained a topic of vivid interest in nuclear structure physics. These 0^+ excited states display structure properties which so far have escaped full understanding. The reason is that low-lying 0^+ levels may be formed in many different ways.

Among the models proposed to describe the structure of the excited 0^+ states, that proposed several decades ago by Bohr and Mottelson [1] rests on the picture of quadrupole shape vibration taking place along the nuclear symmetry axis in deformed nuclei. The concept of β vibration associated with 0_2^+ levels was thus highlighted. The validity of this model has essentially been challenged in the rare-earth region. It has been shown that 0_2^+ excited states generally are not β vibrations [2].

Progress in the understanding of 0_2^+ states and related electric monopole $E0(0_2^+ \rightarrow 0_1^+)$ transitions was achieved based on the interacting boson model (IBA) [3]. For example, it was shown using IBA calculations that sharp rises observed for the $\rho^2(E0; 0_2^+ \rightarrow 0_1^+)$ transition strengths in the mass regions $A \approx 100$ and $A \approx 150$ are related to shape and phase transitions [4]. Shape transition and shape coexistence as well as phase transition pictures are the hallmarks

of present day understanding of $E0(0_2^+ \rightarrow 0_1^+)$ transitions and related phenomena [5–8]. The present work provides a systematic comparison between experimental data available for $\rho^2(E0; 0_2^+ \rightarrow 0_1^+)$ transition strengths in even-even nuclei, and five-dimensional collective quadrupole Hamiltonian (5DCH) calculations based on the Gogny force. The calculated $\rho^2(E0)$ values reported in [9] are generally too strong, as pointed out in [10] and [11]. Modeling has been improved following prescriptions and methods outlined below.

The paper is organized as follows. Sec. II first includes a reminder of 5DCH formalism. Next we outline a method [12] which takes into account symmetry properties of the Bohr Hamiltonian [13] to build the 5DCH kinetic tensor. As a consequence, vibrational mass parameters get stronger than those inferred from the Inglis-Beliaev (IB) approximation and are considered here as “renormalized.” Finally, the Church and Weneser (CW) $E0$ transition operator is introduced [14]. Sensitivity calculations are discussed in Sec. III. These include comparisons between predictions based on (i) D1S [15] and D1M [16] Gogny forces, (ii) IB and renormalized collective masses, and (iii) CW and standard (S) prescriptions for the $E0$ transition operator. Once the best strategy is adopted, systematic investigations of $\rho^2(E0; 0_2^+ \rightarrow 0_1^+)$ values are performed from neutron number N running from drip line to drip line and for nuclei with proton numbers $10 \leq Z \leq 100$. This leads to the identification of regions where $\rho^2(E0; 0_2^+ \rightarrow 0_1^+)$ values calculated over (Z, N) display a maximum. Sections IV and V are devoted to systematic analyses of $\rho^2(E0)$ and $X(E0/E2)$

*marc.dupuis@cea.fr

data, respectively. In Sec. VI we discuss the $E0$ decay properties of the 0_2^+ and 0_3^+ levels in ^{238}U . This study has been an opportunity to combine 5DCH and quasiparticle random phase approximation (QRPA) approaches. Section VII is devoted to $\rho^2(E0)$ properties of the $0_2^+ \rightarrow 0_1^+$, $0_3^+ \rightarrow 0_1^+$, and $0_4^+ \rightarrow 0_1^+$ transitions in ^{166}Er using both microscopic methods. $E2$ transitions are discussed too in the context of the 5DCH model, in an attempt to elucidate structure properties of this Er isotope. Finally, a summary as well as suggestions intended to globally achieve improved $\rho^2(E0; 0_2^+ \rightarrow 0_1^+)$ and $X(E0/E2)$ microscopic model predictions are offered in Sec. VIII.

II. REMINDER OF THE 5DCH FORMALISM AND ELECTRIC MONOPOLE TRANSITION

A. 5DCH Hamiltonian

The collective Hamiltonian in five quadrupole coordinates results from the generator coordinate method treated in the Gaussian overlap approximation. For details, see Refs. [9,17]. The 5DCH Hamiltonian is written as

$$\widehat{\mathcal{H}} = -\frac{\hbar^2}{2} \sum_{ij} \frac{\partial}{\partial q_i} [M^{-1}(q)]_{ij} \frac{\partial}{\partial q_j} + \mathcal{V}(q) \quad (1)$$

with $q_i = (q_0, q_2)$, where q_0 and q_2 stand for axial and triaxial deformations, respectively, and with the three Euler angles. $M^{-1}(q)$ and $\mathcal{V}(q)$ are the tensor of inertia and potential energy surface corrected for zero-point energy [17]. The collective masses $B_{ij}(q)$ and moments of inertia $\mathcal{J}_k(q)$ entering the tensor of inertia were initially calculated in the cranking approximation [18,19]. Remarkably the collective masses and moments of inertia calculated in the Inglis-Beljaev (IB) approximation fulfill symmetry properties of the collective Hamiltonian $\widehat{\mathcal{H}}$ on its symmetry axes [13]. These properties are discussed in [12].

B. Collective masses

It is an important goal of the present work to release the IB approximation in the determination of collective masses. This is achieved by taking advantage of the symmetry properties of the collective Hamiltonian $\widehat{\mathcal{H}}$, in which the IB moments of inertia are now replaced by those determined in self-consistent cranking calculations [9,20]. Such cranking moments of inertia are equivalent to Thouless-Valatin (TV) moments of inertia [21]. As the TV moments of inertia are stronger than those based on the IB approximation, it is anticipated that the values of renormalized collective masses will get stronger. The process by which renormalized collective masses are built is explained in [12]. Such stronger collective mass values resulting from controlled approximations lead to minor effects on 5DCH predictions for the first 0^+ excited state energies ($E0_2^+$) calculated in [9]. These ($E0_2^+$) energies were systematically 50% high. The renormalized masses (Re) do not modify this general feature, except for deformed rotational nuclei [12] where 0_2^+ excitation energies get reduced by typically 10%.

C. $E0$ transitions

According to Church and Weneser [14] the electric monopole strength, labeled as CW in the following discussions, has the general form

$$\rho^2(E0; 0_2^+ \rightarrow 0_1^+) = \left| \frac{\langle 0_2^+ | \sum_{i=1}^Z (e_i r_i)^2 | 0_1^+ \rangle}{R^2} \right|^2 - \sigma \left| \frac{\langle 0_2^+ | \sum_{i=1}^Z (e_i r_i)^2 | 0_1^+ \rangle}{R^2} \right|^4, \quad (2)$$

where R is an effective radius, $R = 1.2A^{1/3}$ fm, r_i the radius of the i th proton, and e_i the effective charge. In this work no effective charge is assumed, i.e., $e_i = 1.0$. The numerical coefficient σ was estimated to take on the value $\lesssim 0.1$ [14]. The actual value we have adopted throughout the calculations is $\sigma = 0.1$. Equation (2) reduces to the well known form

$$\rho^2(E0; 0_2^+ \rightarrow 0_1^+) = \left| \frac{\langle 0_2^+ | \sum_{i=1}^Z (e_i r_i)^2 | 0_1^+ \rangle}{R^2} \right|^2 \quad (3)$$

when σ is assumed to be null, the choice made earlier in [22]. In the following, this form, Eq. (3), is designated as standard (S).

The dimensionless parameter $X(E0/E2)$ is often taken in current literature as a measure of $E0$ transition strength. X is defined as the ratio between reduced transition probabilities for monopole ($E0$) and quadrupole ($E2$) transitions. According to Rasmussen [23], this ratio is written as

$$X(E0/E2) = e^2 R^4 \frac{\rho^2(E0; 0_2^+ \rightarrow 0_1^+)}{B(E2; 0_2^+ \rightarrow 2_1^+)}, \quad (4)$$

where 2_1^+ is the first 2^+ excited state in a nucleus. The value $e = 1.0$ is adopted.

III. SENSITIVITY STUDIES

As the $\rho^2(E0)$ values calculated in [9] are known to be much larger than experiment [10,11], sensitivity calculations have been performed. These tests are intended to identify which inputs to 5DCH model are keys for lowering the values taken by the calculated $E0$ transition strengths.

A. D1S versus D1M

The first sensitivity tests focused on changing Gogny force parametrization from D1S [15,24] to D1M [16] in the calculations. D1M is an effective force that displays an incompressibility modulus K_∞ stronger than that of D1S, namely $K_\infty = 203$ MeV and $K_\infty = 225$ MeV for D1S and D1M, respectively. The influence of changing force is displayed in Figs. 1 and 2, showing illustrations for $Z = 40$ isotopes and $N = 40$ isotones, respectively. Panels (a) and (b) in the two figures are for excitation energies of first 0^+ excited states and for $\rho^2(E0)$ values, respectively. Full circles are for experimental values [25], blue and green symbols are for D1S and D1M calculations, respectively.

It is seen in Fig. 1(a) that experimental and calculated values display a maximum at the $N = 50$ shell closure. As

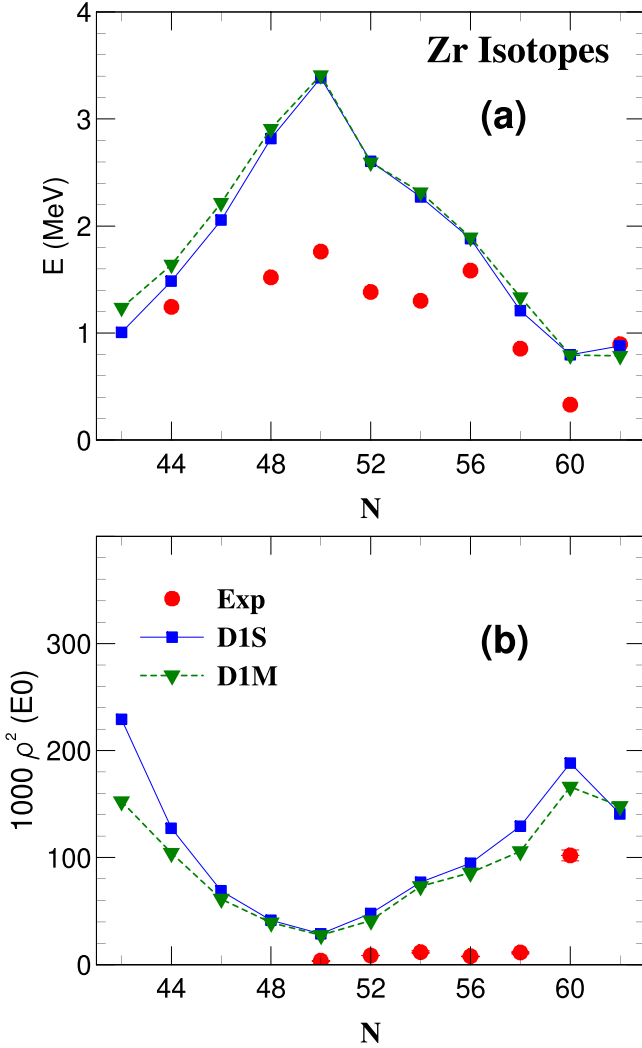


FIG. 1. $Z = 40$ isotopes. (a) Excitation energies (MeV) of first 0^+ excited states as functions of neutron number N . (b) Squares of monopole transition strengths times 1000, $1000\rho^2(E0)$, for the $0_2^+ \rightarrow 0_1^+$ transition as functions of N . In both panels, red circles are for experimental data. Blue and green curves are for 5DCH calculations involving the D1S and D1M forces, respectively. Calculations are performed using collective masses determined at the level of the Inglis-Beliaev approximation. The $E0$ transition operator is that of Church and Weneser reduced to its first component.

anticipated from 5DCH calculations performed at and in the vicinity of closed shells, calculated energies are much larger than experiment for $N \approx 50$. The experimental $\rho^2(E0)$ values display a sharp increase at $N = 60$. In contrast, the $\rho^2(E0)$ values calculated using D1S and D1M forces display a gradual increase with increasing N values, and show a maximum for $N = 60$. This feature displayed by the blue and green curves is the signature of a nuclear transition from spherical ($N = 50$) to deformed ($N = 60$) shapes, also named the first-order phase transition [6,7]. In Fig. 1(b) one can also observe colored curves showing increases with N decreasing below $N = 50$. The maximum of $\rho^2(E0)$ values takes place for $N \approx 40$, that

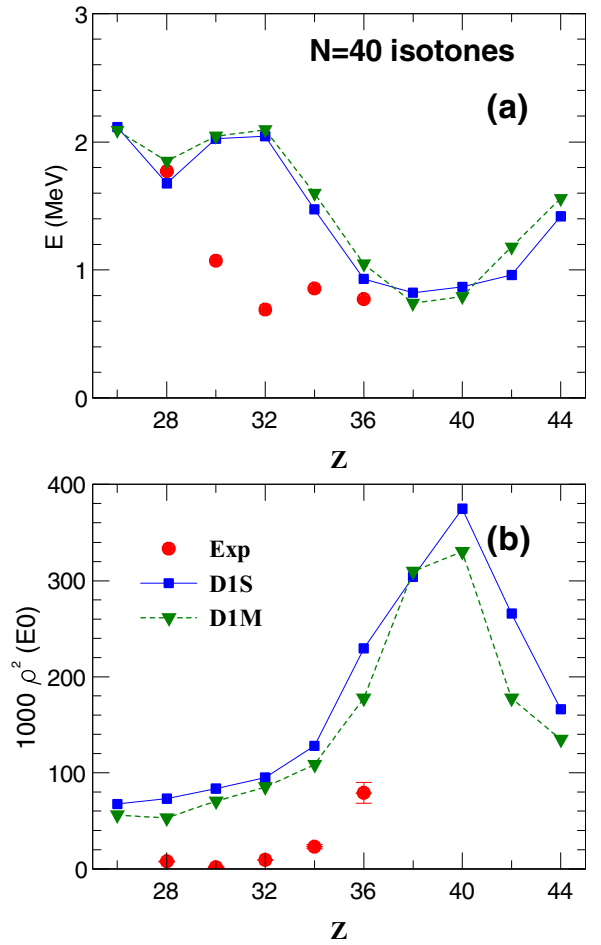


FIG. 2. $N = 40$ isotones. (a) Excitation energies (MeV) of first 0^+ excited states as functions of charge number Z . (b) Squares of monopole transition strengths times 1000, $1000\rho^2(E0)$, for the $0_2^+ \rightarrow 0_1^+$ transition as functions of Z . In both panels, red circles are for experimental data. Blue and green curves are for 5DCH calculations involving the D1S and D1M forces, respectively. For other information see caption of Fig. 1

is for the isotope ^{80}Zr which is strongly deformed [26] and located near the proton drip line.

Panel (a) in Fig. 2 shows the five 0^+ excitation energies for the $N = 40$ isotopes [25] as red symbols. The blue and green symbols are for calculations performed using the D1S and D1M forces, respectively. The two colored curves are much higher than experiments for the isotones with proton numbers $Z = 30, 32,$ and 34 . This feature, already discussed in [27], most likely is related to the fragile nature of the $N = 40$ subshell closure. Figure 2(b) shows experimental and calculated $\rho^2(E0)$ values. The experimental values (red symbols) increase gradually with increasing Z , as do the two sets of calculated values.

On the basis of (i) $\rho^2(E0)$ calculated values and comparisons with experimental data [28] shown above, and (ii) similar comparisons performed in higher mass regions, we conclude that the D1S and D1M forces lead to similar predictions. However, smaller $\rho^2(E0)$ values calculated using

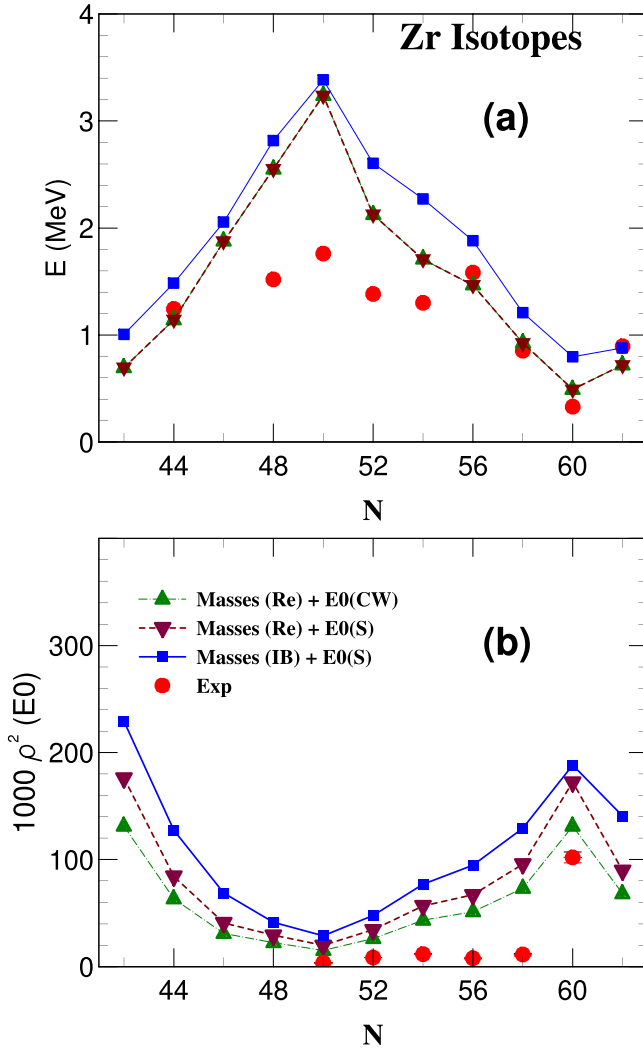


FIG. 3. Zr isotopes. (a) Excitation energies (MeV) of first 0^+ excited states as functions of neutron number N . (b) Squares of monopole transition strengths times 1000, $1000\rho^2(E0)$, for the $0_2^+ \rightarrow 0_1^+$ transition as functions of N . In both panels, red circles are for experimental data. Blue curves are for 5DCH calculations performed involving collective masses determined in the Inglis-Beliaev approximation, and the $E0$ transition operator reduced to its first component. Green triangles in panels (a) and (b) are for 5DCH calculations performed using renormalized collective masses (see main text) and the $E0$ transition operator reduced to its first component. Green triangles in panel (b) are for 5DCH calculations performed using renormalized collective masses and full $E0$ transition operator.

D1M seem directly related to the higher stiffness content of the force. Here, we will perform all the following 5DCH calculations using only D1S.

B. Evaluation of vibrational mass parameters and $E0$ operator

We next discuss the way collective masses renormalization influences the strength of calculated $\rho^2(E0)$, assuming either the standard $E0$ transition operator, Eq. (3), or the Church and Weneser $E0$ operator, Eq. (2). Illustrations are provided in Figs. 3 and 4 for the Zr isotopes and for $N = 82$ isotones,

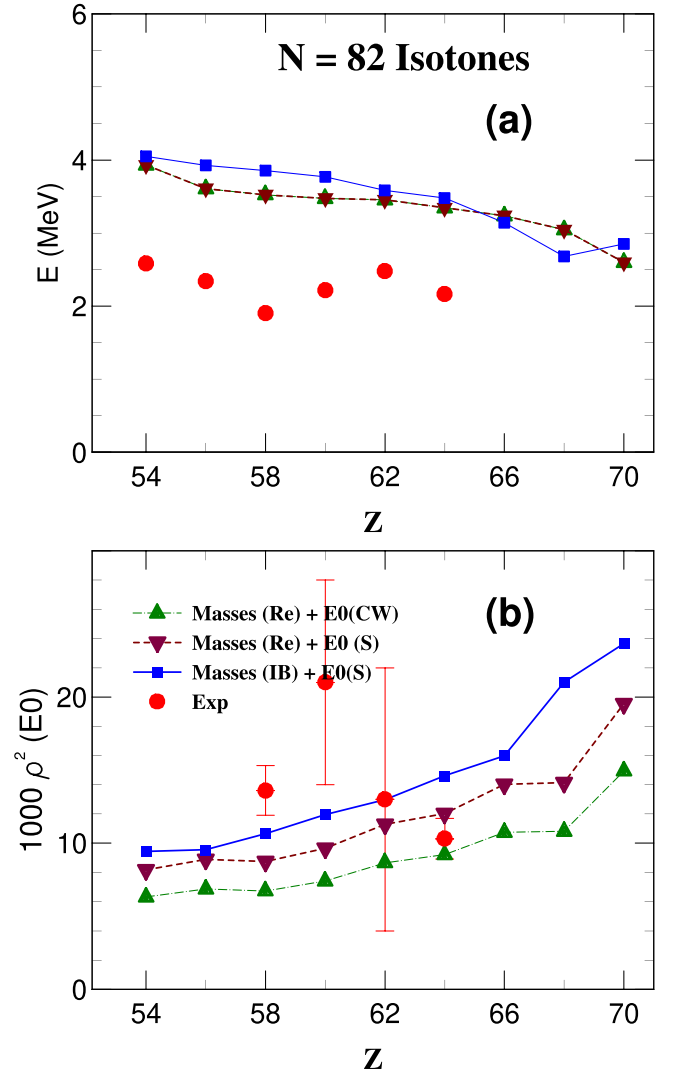


FIG. 4. $N = 82$ isotones. (a) Excitation energies (MeV) of first 0^+ excited states as functions of proton number Z . (b) Squares of monopole transition strengths times 1000, $1000\rho^2(E0; 0_2^+ \rightarrow 0_1^+)$, as functions of Z . In both panels, red circles are for experimental data. Blue curves are for 5DCH calculations performed involving collective masses determined in the Inglis-Beliaev approximation and the $E0$ transition operator reduced to its first component. Pink triangles in panels (a) and (b) are for 5DCH calculations performed using renormalized collective masses (see main text) and the $E0$ transition operator reduced to its first component. Green triangles are for renormalized collective masses and full $E0$ transition operator.

respectively. The figures are organized in a manner similar to that adopted for Figs. 1 and 2.

Figures 3(a) and 3(b) show experimental data as red circles. Blue symbols and curves are for 5DCH calculations in which Inglis-Beliaev (IB) collective masses and the standard $E0$ transition operator [$E0(S)$] are involved. Brown symbols and curves are for renormalized masses (Re) and $E0(S)$ operator. Finally, green symbols and curves are for renormalized masses and the Church and Weneser (CW) $E0$ transition operator. In Fig. 3(a) we see that renormalized masses are systematically lowering the excitation energies ($E0_2^+$). The

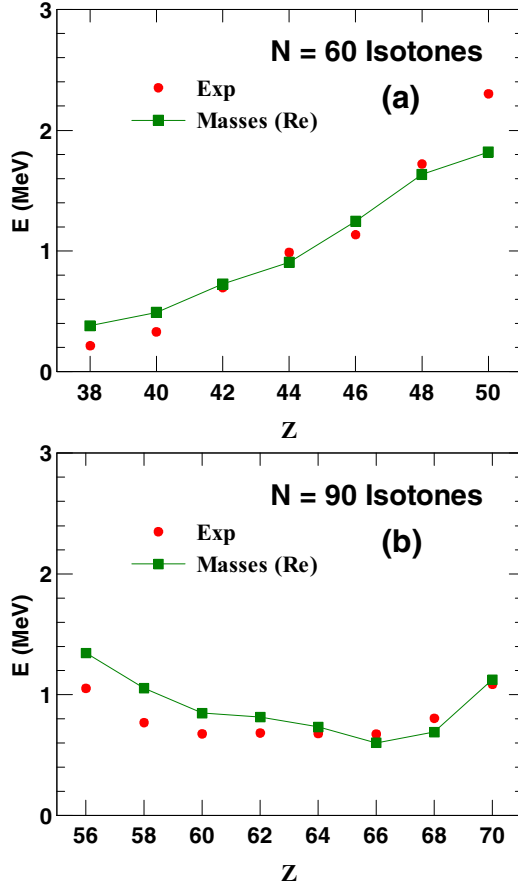


FIG. 5. Excitation energies (MeV) of first 0^+ excited states in $N = 60$ and $N = 90$ isotones are shown in panels (a) and (b), respectively. Experimental values (red circles) and results from 5DCH calculations (green squares) involving renormalized masses that are labelled as Masses (Re).

reduction in $\rho^2(E0)$ values, see Fig. 3(b), is at a maximum when using renormalized masses and full $E0$ transition operator. Similar 5DCH calculations are shown in Figs. 4(a) and 4(b) for $N = 82$ isotones. As expected, all the predicted ($E0_2^+$) energies stand much higher than measurements at this neutron shell closure. The red, blue, brown, and green symbols have the same meaning as in Fig. 3. Again, renormalized masses and full $E0$ transition operator lead to maximum reduction in the predicted $\rho^2(E0)$ values. These values are representative of the average value taken by data, which display large error bars.

As a final comment on sensitivity studies, data for excitation energies of first excited states (0_2^+) in $N = 60$ and $N = 90$ isotones are shown as red circles in panels (a) and (b), respectively, of Fig. 5. For open-shell nuclei, the calculated 0_2^+ values (green squares) based on 5DCH calculations performed with renormalized masses match rather well the measurements.

C. ($E0_2^+$) energy distribution over Z and N

The 5DCH calculations based on D1S force were performed for ($E0_2^+$) energies and $\rho^2(E0)$ strengths in even-even

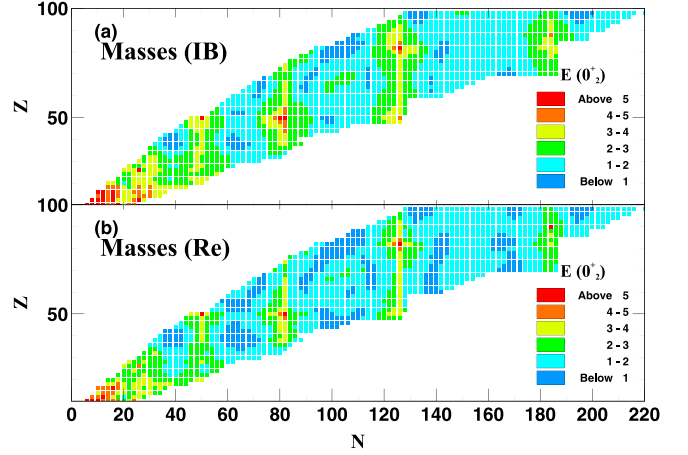


FIG. 6. Energies (MeV) of first 0^+ excited states from 5DCH calculations over proton numbers $10 < Z < 100$ and neutron numbers $N < 220$. The color code is for calculated excitation energies. Panels (a) and (b) are for 5DCH calculations involving Inglis-Beljaev collective masses and normalized collective masses, respectively.

nuclei with masses spreading from proton to neutron drip line. Our aim was the identification of minima present in energies and maxima in $\rho^2(E0)$'s over the (Z, N) mass region defined by the proton number $10 \leq Z \leq 100$.

The predictions obtained for energies are shown in Fig. 6. Panels (a) and (b) are for calculations conducted assuming the standard $E0$ transition operator. Panel (a) is for predictions based on Inglis-Beljaev collective masses, and panel (b) for calculations performed using renormalized masses. The two sets of energy predictions are similar. The distribution of color symbols indicates energy range, from ($E0_2^+$) < 1 MeV (dark blue) to ($E0_2^+$) > 5 MeV (magenta). The regions where energies are lowest are predicted for $(Z, N) \approx (38, 40)$, $(38, 62)$, $(60, 72)$, $(60, 90)$, $(76, 100)$, and $(96, 134)$. These groups in excitation energies more or less coincide with those in the classification provided in Table VII of [6]. The lowest calculated energies located in the group $(Z, N) \approx (60, 72)$ were identified previously by the present authors [29] in neutron deficient Nd isotopes. For these isotopes, the calculated $1000\rho^2(E0)$ strengths take on large values in the vicinity of the neutron drip line.

D. $\rho^2(E0)$ strength distribution over Z and N

Figure 7 shows predictions for $\rho^2(E0)$ obtained using the standard $E0$ transition operator in calculations similar to those presented in Fig. 6 for energies. Panels (a) and (b) are for results based on Inglis-Beljaev collective masses and renormalized masses, respectively. The color symbols are for strengths ranging from small (blue color) to strong (red) values. Strong values, with $1000\rho^2(E0) > 150$, are seen in several groups, namely for $(Z, N) \approx (38, 40)$, $(38, 60)$, $(60, 64)$, $(60, 90)$, $(76, 100)$, and $(96, 148)$, in panels (a) and (b). The maxima identified in $1000\rho^2(E0)$ values over Z and N closely coincide with minima located in excitation energies ($E0_2^+$) for similar Z and N values. Systematic $\rho^2(E0)$ calculations over Z and N , involving the full CW $E0$ transition

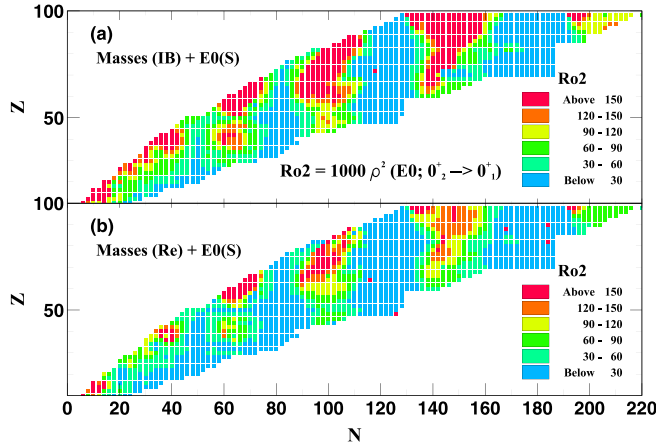


FIG. 7. Squares of $E0$ transition strength times 1000, $1000\rho^2(E0; 0_2^+ \rightarrow 0_1^+)$, as provided by 5DCH calculations performed for nuclides with $10 < Z < 100$ and $N < 220$. Panels (a) and (b) are for 5DCH calculations involving Inglis-Beljaev collective masses and normalized collective masses, respectively. The color code is intended to indicate strength magnitudes.

operator, have not been performed. In spite of this fact, the various sensitivity studies presented so far lead to the conclusion that (i) renormalized collective masses in combination with (ii) the Church and Weneser $E0$ transition operator systematically reduce and improve $\rho^2(E0)$ value predictions when implemented in the 5DCH calculations. It is this combination of collective masses and $E0$ operator that will be adopted below in systematic 5DCH calculations performed for many $\rho^2(E0; 0_2^+ \rightarrow 0_1^+)$ and $X(E0/E2)$ values.

IV. ANALYSES OF $\rho^2(E0)$ DATA

We focus on detailed comparisons between the experimental $1000\rho^2(E0)$ values with our calculations performed for the following regions: (i) the medium-mass Se, Kr, Zr, Mo, Pd, and Cd isotopes and (ii) isotopes in the rare-earth region as well as those with higher charge numbers $Z < 72$. The ^{238}U isotope is also considered. The database, which comprises 52 nuclei, was formed based on the compilation [28]. It also includes the publication [30] for ^{238}U .

A. Se, Kr, Zr, Mo, Pd, and Cd isotopes

Panels (a) to (f) of Fig. 8 show $1000\rho^2(E0)$ data (red symbols) and 5DCH predictions (green curves) for Se, Kr, Zr, Mo, Pd, and Cd isotopes, respectively. The predicted $1000\rho^2(E0)$ values are generally high compared to data. This is especially relevant to the Kr isotopes, where the peak seen at $N = 38$ in experimental and calculated values for the $E0$ transition strength is associated with a transition from prolate to oblate shapes when N decreases from $N = 40$ to $N = 36$ [22]. Symmetry-conserving configuration-mixing calculations dedicated to $\rho^2(E0)$ values for the Kr isotopes also overshoot measurements [31]. The nucleus ^{72}Kr is the isotope for which the $1000\rho^2(E0)$ value from 5DCH calculation now matches the data. Panel (c) for Zr isotopes includes $1000\rho^2(E0)$ values calculated for ten neutron

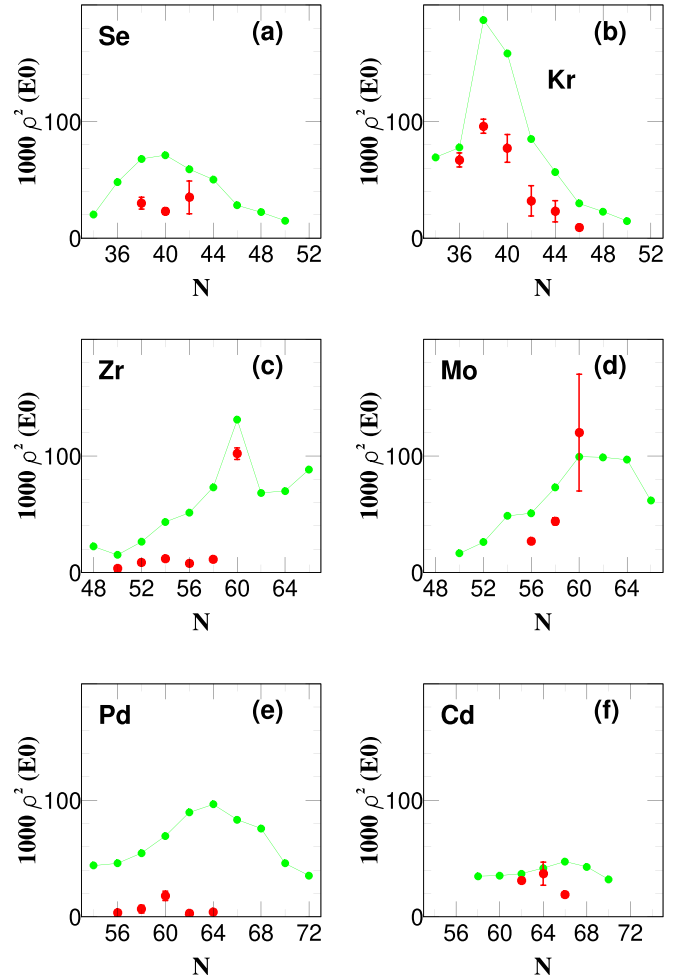


FIG. 8. $1000\rho^2(E0; 0_2^+ \rightarrow 0_1^+)$ experimental values for Se, Kr, Zr, Mo, Pd, and Cd isotopic chains are shown in panels (a), (b), (c), (d), (e), and (f), respectively. The green symbols are for 5DCH calculations performed using renormalized collective masses and full $E0$ transition operator.

numbers N , with $48 \leq N \leq 66$. Both data and calculations clearly illustrate the occurrence of the phase transition at $N = 60$. This phase transition at $N = 60$ does not take place for the adjacent Mo isotopes, as can be seen in panel (d). These features indicate that the phase transition in the medium mass region is specific to the $Z = 40$ isotopes. Panel (f) shows $1000\rho^2(E0)$ data and calculated values for Cd isotopes. Only the experimental value at $N = 64$ is reasonably well described by prediction. Cd isotopes are known to display shape coexistence phenomena, as discussed in extensive comparisons between recent $B(E2)$ measurements and symmetry-conserving configuration-mixing calculations [32]. In particular, the collective band built on top of the first 0^+ excited state is found to be more deformed than that based on the ground state. 5DCH calculations for the Cd isotopes lead to similar nuclear structure properties [9,33]. Taking ^{112}Cd as an illustration, the calculated mean axial and triaxial quadrupole deformations (β) and (γ), respectively, are (β) = 0.21 and (γ) = 26° for the ground state. For the 0_2^+ level, the mean deformations are (β) = 0.33 and (γ) = 16° , which means

that this excited 0^+ state is $\approx 57\%$ more deformed and also less triaxial than the ground state.

The qualitative agreement between $\rho^2(E0)$ data and calculations for Pd isotopes is poor; see panel (e). It is also puzzling since Pd isotopes, as seen above for Cd isotopes, also display shape coexistence in the present 5DCH predictions. For example, the mean $\langle\beta\rangle$ and $\langle\gamma\rangle$ deformations calculated for ground state and 0_2^+ levels of ^{110}Pd are $\langle\beta\rangle = 0.27$, $\langle\gamma\rangle = 23^\circ$ and $\langle\beta\rangle = 0.32$, $\langle\gamma\rangle = 20^\circ$, respectively. The degree of coexistence in Pd isotopes might be considered lower when compared to that in Cd, since the difference in mean $\langle\beta\rangle$ deformations associated with the 0_1^+ and 0_2^+ levels is of the order of 20%. This smaller degree of coexistence might explain why the experimental $\rho^2(E0)$ data for Pd isotopes are smaller than those for Cd isotopes. On the other hand we do not understand the reasons why the calculated $\rho^2(E0)$ values for Pd, with four protons less than Sn at the shell closure $Z = 50$, are stronger than those for Cd. We suggest that the Gogny energy density functional would lead to improved predictions if it were implemented with two-quasiparticle (2qp) components. We will refer to this suggestion, aimed at improving various predictions, later in this study.

B. Sn, Nd, Sm, Gd, Er, and Yb isotopes

Panels (a) to (f) of Fig. 9 show $1000\rho^2(E0)$ data (red symbols) and 5DCH predictions (green curves) for Sn, Nd, Sm, Gd, Er, and Yb isotopes, respectively. The $\rho^2(E0)$ data and predictions for proton- closed shell Sn isotopes are shown in panel (a). When comparing the Sn and Cd data we notice similarity in trends versus increasing N , and lower values for $N > 64$ ($N = 64$ is at mid neutron shell). Like Cd isotopes, Sn isotopes display shape coexistence [34]. The calculations reproduce reasonably well $\rho^2(E0)$ data for $N < 66$, but stand too high for higher N values. This feature is similar to that observed for Cd isotopes. This caveat points again to a deficiency in the present modeling. The calculated $\rho^2(E0)$ values (green curves) for Nd, Sm, and Gd isotopes display similar characteristics in the vicinity of $N = 90$: a maximum followed immediately by a lower value for $N = 92$. In the three isotopic chains, transitions from spherical to deformed shapes take place when the neutron number increases above $N = 82$. This feature indicates a quantum phase transition at $N = 90$ [35,36]. It is interesting to note that, for the Nd isotopes, our calculated $\rho^2(E0)$ values look similar in shape and magnitude to those calculated using a relativistic effective force as published in [37]. The Gd isotopes display similar features in measured and calculated $\rho^2(E0)$ values in the vicinity of $N = 90$.

For the Nd isotopes, $\rho^2(E0)$ measurements are needed to strengthen the picture of quantum phase transition at $N = 90$. A phase transition at or near this neutron number is well established based on quadrupole transition properties [38]. In the present work, we have considered as complementary information the ratio between 5DCH values $B(E2; 2_2^+ \rightarrow 0_1^+)/B(E2; 2_2^+ \text{ or } 2_3^+ \rightarrow 0_2^+)$ among reduced transition probabilities determined for $N = 88, 90$, and 92 isotopes of the elements Nd, Sm, Gd, Dy, and Er. The calculated $B(E2; 2_3^+ \rightarrow 0_2^+)$ value is ignored whenever $B(E2; 2_2^+ \rightarrow 0_2^+)$ is stronger,

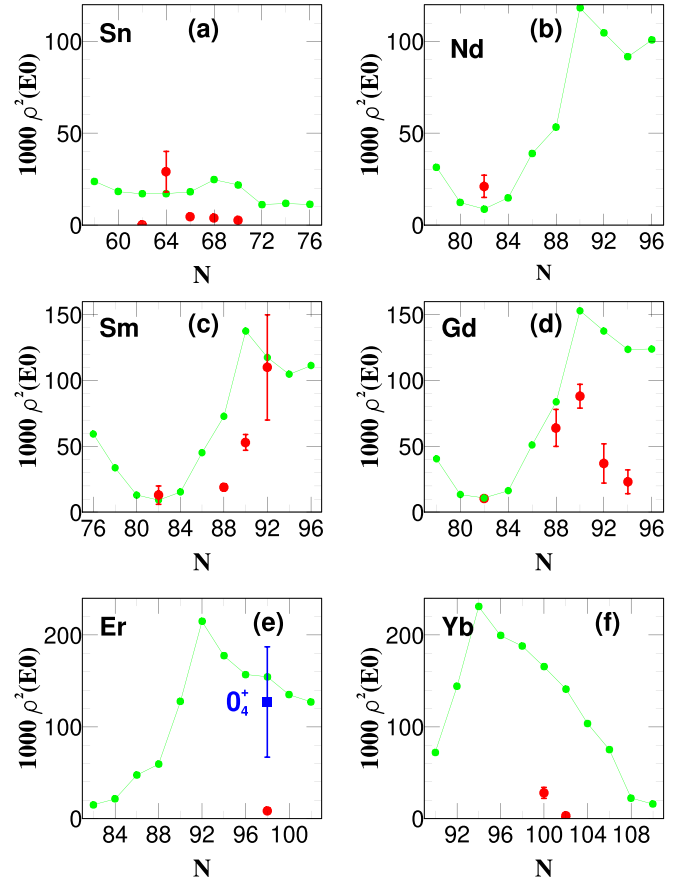


FIG. 9. $1000\rho^2(E0; 0_2^+ \rightarrow 0_1^+)$ experimental values for Sn, Nd, Sm, Gd, Er, and Yb isotopic chains are shown in panels (a), (b), (c), (d), (e), and (f), respectively. The green symbols are for 5DCH calculations performed using renormalized collective masses and full $E0$ transition operator. The blue symbol is for the experimental $\rho^2(E0; 0_4^+ \rightarrow 0_1^+)$ value.

and the reverse otherwise. The calculated $B(E2)$ ratios, shown in Table I, display a maximum greater than unity for $N \approx 90$.

Panels (e) and (f) display $\rho^2(E0; 0_2^+ \rightarrow 0_1^+)$ data (red circles) obtained at a few neutron numbers: $N = 98$ and $N = 102, 104$ for Er and Yb nuclei, respectively. These values are very small as compared to predictions, which peak at values $1000\rho^2(E0) \approx 220$. It is tempting to suggest that the $E0$ strengths as obtained from 5DCH calculations in this higher mass region are fragmented over several excited 0^+ levels taking place at a few MeV of excitation energy. In recent years, many (p, t) pickup reactions aimed at the identification of 0^+ levels below approximately 3 MeV have collected unprecedented numbers of such excitations in rare-earth nuclei [39]. An alternative suggestion would be that the experimental data (red circles) in panels (e) and (f) stem from 2qp excitations, a picture that is not compatible with that conveyed by the 5DCH model. Instead, systematic QRPA calculations based on D1S might be suitable to describe the low $\rho^2(E0; 0_2^+ \rightarrow 0_1^+)$ values measured in the rare-earth region.

Figure 9(e) shows a second $\rho^2(E0)$ measurement, again for the ^{166}Er isotope. The $\rho^2(E0)$ value, namely $1000\rho^2(E0) = 127(60)$, is represented by a blue square and large error bar.

TABLE I. The third column shows 5DCH values (in Weisskopf units) of $E2$ reduced transition probabilities $B(E2; 2_1^+ \rightarrow 0_1^+)$, $B(E2; 2_2^+ \rightarrow 0_2^+)$, and/or $B(E2; 2_3^+ \rightarrow 0_2^+)$ for the Nd, Sm, Gd, Dy, and Er isotopes with neutron numbers $N = 88, 90, 92$. $B(E2)$ ratios $B(E2; 2_i^+ \rightarrow 0_2^+)/B(E2; 2_1^+ \rightarrow 0_1^+)$, $i = 2$ or 3 , between calculated values are given in the fourth column. Experimental ratio values are shown in the fifth column.

Nucleus	Transition	$B(E2 \downarrow)$ (W.u.)	$B(E2)$ ratio DIS	$B(E2)$ ratio expt.
$^{148}\text{Nd}_{88}$	$2_1^+ \rightarrow 0_1^+$	64.92	0.83	
	$2_3^+ \rightarrow 0_2^+$	78.44		
$^{150}\text{Nd}_{90}$	$2_1^+ \rightarrow 0_1^+$	117.39	1.00	1.38 (15)
	$2_2^+ \rightarrow 0_2^+$	117.20		
$^{152}\text{Nd}_{92}$	$2_1^+ \rightarrow 0_1^+$	155.54	1.09	
	$2_2^+ \rightarrow 0_2^+$	142.98		
$^{150}\text{Sm}_{88}$	$2_1^+ \rightarrow 0_1^+$	76.95	0.92	
	$2_3^+ \rightarrow 0_2^+$	83.58		
$^{152}\text{Sm}_{90}$	$2_1^+ \rightarrow 0_1^+$	146.16	1.10	1.17 (21)
	$2_2^+ \rightarrow 0_2^+$	132.73		
$^{154}\text{Sm}_{92}$	$2_1^+ \rightarrow 0_1^+$	175.63	1.19	
	$2_2^+ \rightarrow 0_2^+$	148.14		
$^{152}\text{Gd}_{88}$	$2_1^+ \rightarrow 0_1^+$	85.33	0.95	
	$2_3^+ \rightarrow 0_2^+$	89.38		
$^{154}\text{Gd}_{90}$	$2_1^+ \rightarrow 0_1^+$	158.46	1.11	0.62 (7)
	$2_2^+ \rightarrow 0_2^+$	143.32		
$^{156}\text{Gd}_{92}$	$2_1^+ \rightarrow 0_1^+$	189.97	1.05	
	$2_3^+ \rightarrow 0_2^+$	180.89		
$^{154}\text{Dy}_{88}$	$2_1^+ \rightarrow 0_1^+$	84.24	0.68	
	$2_3^+ \rightarrow 0_2^+$	124.68		
$^{156}\text{Dy}_{90}$	$2_1^+ \rightarrow 0_1^+$	157.76	1.10	
	$2_2^+ \rightarrow 0_2^+$	143.67		
$^{158}\text{Dy}_{92}$	$2_1^+ \rightarrow 0_1^+$	202.36	1.05	
	$2_3^+ \rightarrow 0_2^+$	192.90		
$^{156}\text{Er}_{88}$	$2_1^+ \rightarrow 0_1^+$	75.89	0.58	
	$2_3^+ \rightarrow 0_2^+$	130.78		
$^{158}\text{Er}_{90}$	$2_1^+ \rightarrow 0_1^+$	115.94	0.74	
	$2_3^+ \rightarrow 0_2^+$	157.43		
$^{160}\text{Er}_{92}$	$2_1^+ \rightarrow 0_1^+$	190.95	1.05	
	$2_2^+ \rightarrow 0_2^+$	183.55		

It is related to the $E0(0_4^+ \rightarrow 0_1^+)$ transition from the third excited level ($E_x = 1.934$ MeV) to the ground state [40]. This strong value points to the existence of a β vibration, and is compatible with our 5DCH prediction for the $E0(0_2^+ \rightarrow 0_1^+)$ transition strength. A dedicated model interpretation of the $\rho^2(E0; 0_4^+ \rightarrow 0_1^+)$ measurement will be discussed in Sec. VII.

V. ANALYSES OF $X(E0/E2)$ DATA

The database considered for the $X(E0/E2)$ model analyses conducted for the rare-earth and actinide regions comprises 50 values extracted from [28]. As the X data are built as ratios between $B(E0)$ and $B(E2)$ values, we first perform a comparison of $B(E2; 0_2^+ \rightarrow 2_1^+)$ values from measurements with those from the 5DCH calculations.

A. $B(E2)$ values

The $B(E2)$ experimental database includes 41 values, taken mostly from the compilation [25] as of March 30, 2020. Additional values are for ^{94}Zr [41], ^{106}Pd [42], ^{150}Nd [43],

and ^{170}Yb [44]. For ^{152}Gd , we superseded the data with a more recent value; see [45]. Finally, the experimental $B(E2)$ value for ^{168}Yb as quoted in [2] is adopted. The comparison between the $B(E2)$ data and calculated values is shown in Fig. 10. The horizontal axis in panel (a) is for calculations (Th1) performed using IB collective masses. In panel (b), the calculations (Th2) are made using renormalized collective masses. The two models adopted for collective masses do not significantly change the agreement between data and calculations. As can be seen, the calculated values often fall below or above data. The worst situation is for Sn isotopes (brown symbols). It is plausible that present 5DCH modeling for $B(E2)$'s relevant to the single-close-shell Sn isotopes misses consideration of 2qp components.

The deviation between the Th2 values calculated for $B(E2)$ and the experimental data is made by forming the ratio between $B(E2; 0_2^+ \rightarrow 2_1^+)$ (Th2) – $B(E2; 0_2^+ \rightarrow 2_1^+)$ (exp) and $B(E2; 0_2^+ \rightarrow 2_1^+)$ (Th2) for each nucleus under consideration in Fig. 10. Values taken by the ratio are shown in Fig. 11. It can be seen that their mean value over N , $\langle \text{Ratio} \rangle$, is approximately equal to 0.6.

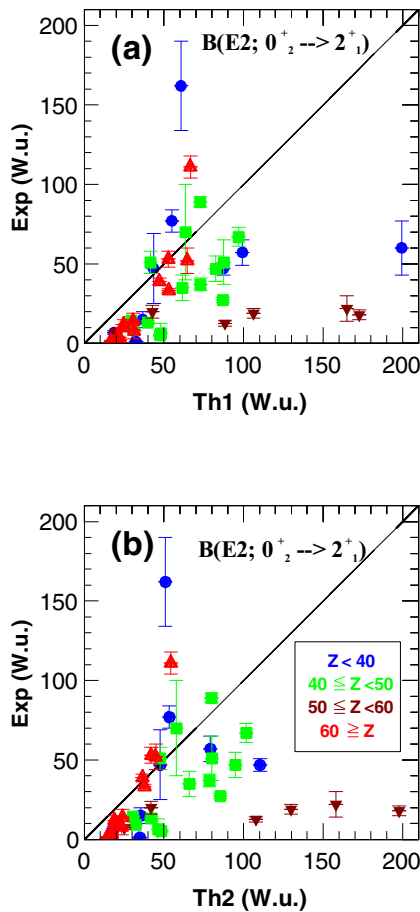


FIG. 10. Comparison between reduced transition probability $B(E2; 0_2^+ \rightarrow 2_1^+)$ from measurements and from 5DCH calculations. Panel (a) shows experimental data compared with calculations (Th1) involving collective masses determined at the Inglis-Beljaev approximation. Panel (b) illustrates similar comparisons, but adopting normalized collective masses in the 5DCH calculations (Th2). The color code is for the identification of proton numbers.

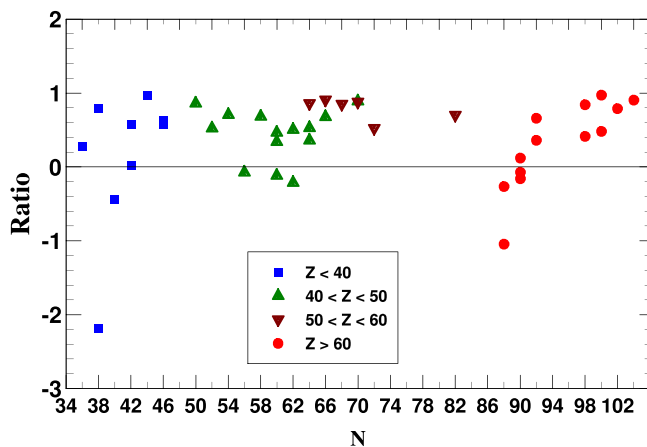


FIG. 11. Difference between the calculated and measured $B(E2; 0_2^+ \rightarrow 2_1^+)$ values, divided by the calculated $B(E2)$ values. This quantity, labeled Ratio, is plotted as a function of neutron number N . The color code is for identification of proton number.

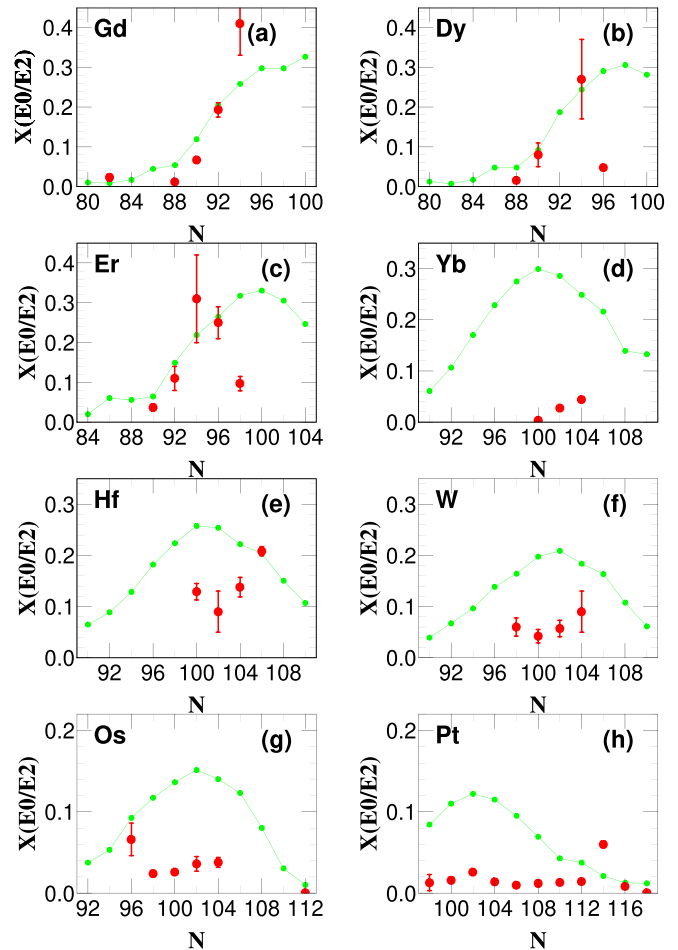


FIG. 12. $X(E0/E2)$ values for Gd, Dy, Er, Yb, Hf, W, Os, and Pt isotopic chains are shown in panels (a) to (h), respectively. Data are shown as red dots. Green curves are for 5DCH calculations performed using renormalized collective masses and full $E0$ transition operator.

B. $X(E0/E2)$ values for Gd, Dy, Er, Yb, Hf, W, Os, and Pt isotopes

The large uncertainties attached to the calculated $B(E2; 0_2^+ \rightarrow 2_1^+)$ values do not spoil the reasonably good agreements between the X data (red circles) and predictions (green points and circles) for the $N < 94$ Gd isotopes, as shown in Fig. 12(a). The $X(E0/E2)$ data increase with N , increasing as do the calculated values until N reaches the value $N = 92$. Agreements of similar quality are obtained for Dy and Er isotopes for neutron numbers $N < 96$ and $N < 98$, in Figs. 12(b) and 12(c), respectively. For higher neutron numbers in these isotopes, the calculated $X(E0/E2)$ values increase and reach a maximum. This pattern is in sharp contrast with the data, whose values drop significantly. For the isotopic chains with higher Z values, the calculated X values form bell shapes over N increasing beyond $N = 92$. In panels (d), (e), (f), (g), and (h) of Fig. 12, we see that reasonable agreement between data and calculations takes place on rare instances. The present 5DCH modeling for $X(E0/E2)$ seems totally inadequate for Yb, Hf, W, Os, and Pt isotopes.

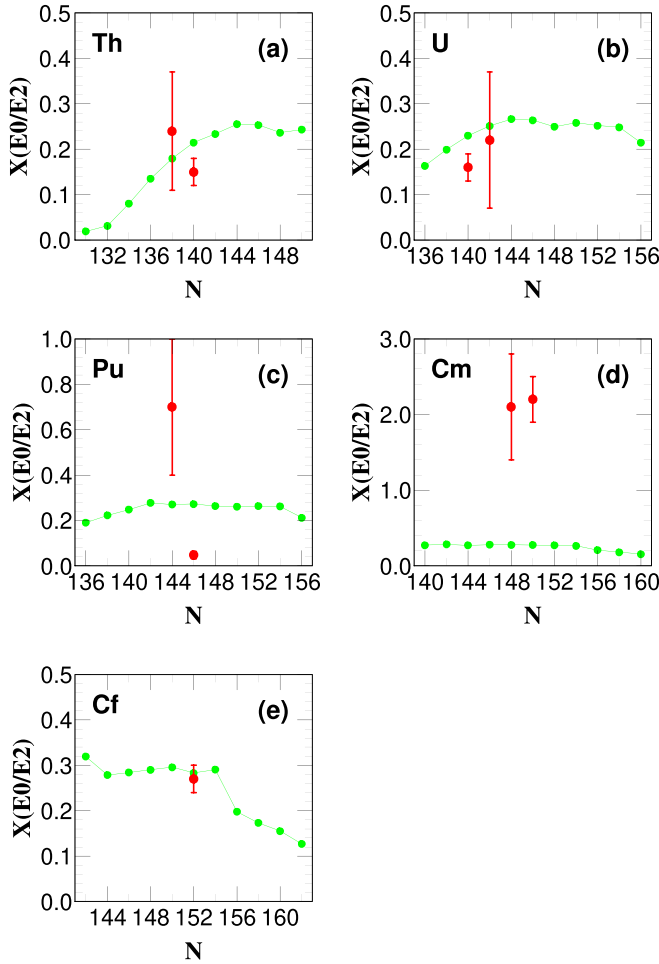


FIG. 13. $X(E0/E2)$ values for Th, U, Pu, Cm, and Cf isotopic chains are shown in panels (a) to (e), respectively. Data are shown as red dots. Green curves are for 5DCH calculations performed using normalized collective masses and full $E0$ transition operator.

C. $X(E0/E2)$ values for Th, U, Pu, Cm, and Cf isotopes

In contrast to the predictions in the medium-mass nuclei, that often fail, we have found reasonable agreements for the actinide region. The experimental data available there are just a few, as can be seen in panels (a), (b), (c), (d), and (e) of Fig. 13 for Th, U, Pu, Cm, and Cf isotopes, respectively. The worst situation is found for Cm isotopes where the experimental values, $X \approx 2$, seem far too strong. For ^{240}Pu , we note that the experimental X value, $X = 0.048(16)$, is very small compared to that measured for the adjacent isotope ^{238}Pu . We noted that ^{240}Pu displays its first excited 0^+ state, which is interpreted as being made of two octupole phonons coupled to null spin [46]. It would be interesting to perform measurements for $E0(0_2^+ \rightarrow 0_1^+)$ and $E0(0_3^+ \rightarrow 0_1^+)$ transitions in this Pu isotope.

VI. $E0$ TRANSITIONS IN ^{238}U

In the actinide mass region we observed two close lying 0^+ excited states, 0_2^+ and 0_3^+ , respectively. They were present in Th and U isotopes at energies near 1 MeV. The actual nature

of such excited states is the topic of an ongoing debate. On the one hand, either one of the two 0^+ excited levels can be interpreted as a two-octupole phonon excitation, according to the *spdf* interacting boson model [46–48]. On the other hand, predictions based on the heavy shell model suggest for the $^{230,232}\text{Th}$ and $^{232,234,236}\text{U}$ isotopes as well as for ^{240}Pu that the 0_3^+ excited state are 2qp excitations [49]. The 0_2^+ levels would then be collective excitations.

As a consequence, it is expected that the $E0$ decay strengths of 0_2^+ and 0_3^+ excited states to 0_1^+ will reflect rather different properties. Such is the case of ^{238}U , for which $\rho^2(E0)$ magnitudes have been measured for the $2_2^+ \rightarrow 2_1^+$ and $2_3^+ \rightarrow 2_1^+$ transitions. Here, the 2_2^+ and 2_3^+ levels are members of the deformed bands built upon the 0_2^+ and 0_3^+ levels, respectively. The experimental $\rho^2(E0)$ and excitation energy values are as follows [30]: $1000\rho^2(E0) = 175(26)$, $E(2_3^+) = 1.037$ MeV and $1000\rho^2(E0) = 9.9(18)$, $E(2_2^+) = 0.966$ MeV for the $2_3^+ \rightarrow 2_1^+$ and $2_2^+ \rightarrow 2_1^+$ transitions, respectively. The energy of the 2_1^+ level is $E(2_1^+) = 44.9$ keV [25].

In the present work, these experimental data are analyzed using the 5DCH model as well as the quasiparticle random phase approximation (QRPA). Here they are used as complementary spectroscopic tools. In recent years, QRPA calculations based on the Gogny force have been performed for dipole transitions [50] and for $0_1^+ \rightarrow I^\pi$ transitions with higher multiplicities [51]. $E0$ predictions based on QRPA and 5DCH have different figures of merit. 5DCH and QRPA calculations turn out to provide best predictions for $\rho^2(E0; 2_3^+ \rightarrow 2_1^+)$ and $\rho^2(E0; 2_2^+ \rightarrow 2_1^+)$ experimental data, respectively.

A. The strong ($2_3^+ \rightarrow 2_1^+$) $E0$ transition

With using the 5DCH approach, we find that $1000\rho^2(E0; 0_3^+ \rightarrow 0_1^+) = 143$. We have also calculated $\rho^2(E0; 2_3^+ \rightarrow 2_1^+)$, and found $\rho^2(E0; 2_3^+ \rightarrow 2_1^+) = \rho^2(E0; 0_3^+ \rightarrow 0_1^+)$ to within a fraction of a percent.

The calculated value $1000\rho^2(E0; 2_3^+ \rightarrow 2_1^+) = 143$ is close to $1000\rho^2(E0; 2_3^+ \rightarrow 2_1^+) = 175(26)$ that is obtained from measurements [30].

B. The weak ($2_2^+ \rightarrow 2_1^+$) $E0$ transition

QRPA calculations based on the D1S Gogny force were performed for the first time using the Church and Weneser $E0$ transition operator. For that purpose, the QRPA wave functions calculated previously for ^{238}U in [52] are adopted. The results for $\rho^2(E0)$ and excitation energy are $1000\rho^2(E0; K^\pi = 0_2^+ \rightarrow K^\pi = 0_1^+) = 34$ and $E(0_2^+) = 1.261$ MeV. Here K is the projection of angular momentum on the third axis, and π is the parity. This 0_2^+ excitation energy is approximately 0.3 MeV higher than the experimental value, namely $E(0_2^+) = 0.966$ MeV.

Assuming that (i) $\rho^2(E0; K^\pi = 0_2^+ \rightarrow K^\pi = 0_1^+)$ is representative of $\rho^2(E0; I^\pi = 0_2^+ \rightarrow I^\pi = 0_1^+)$ and that (ii) $\rho^2(E0; 2_2^+ \rightarrow 2_1^+) = \rho^2(E0; 0_2^+ \rightarrow 0_1^+)$ in the analysis, we deduce that the calculated $\rho^2(E0; 2_2^+ \rightarrow 2_1^+)$ is 73% weaker than that provided by the 5DCH calculations for $\rho^2(E0; 2_3^+ \rightarrow 2_1^+)$. Furthermore, the $1000\rho^2(E0) = 34$ calculated value is

approximately three times stronger than the experimental value: $1000\rho^2(E0) = 9.9(18)$. This mismatch between data and calculation is even stronger considering the revised experimental value [53]: $1000\rho^2(E0; 2_2^+ \rightarrow 2_1^+) = 5.6(22)$.

We conclude that the $E0$ transition associated with the weak $2_2^+ \rightarrow 2_1^+$ transition measured for ^{238}U most likely is a 2qp transition.

VII. $E0$ AND $E2$ TRANSITIONS in ^{166}Er

A. $E0$ transitions

We first consider available $\rho^2(E0)$ data and comparisons with present 5DCH as well QRPA predictions. As can be seen in Fig. 9(e), the calculated $\rho^2(E0; 0_2^+ \rightarrow 0_1^+)$, i.e., $1000\rho^2(E0; 0_2^+ \rightarrow 0_1^+) = 154.4$, is 50 times stronger than the experimental value: $1000\rho^2(E0; 0_2^+ \rightarrow 0_1^+) = 2.2(8)$, shown as a red dot. Also shown on this figure is the experimental $1000\rho^2(E0; 0_4^+ \rightarrow 0_1^+)$, i.e., $1000\rho^2(E0; 0_4^+ \rightarrow 0_1^+) = 127(60)$, deduced from recent measurements [40]. This latter experimental value is of the same magnitude as, and consistent with, the calculated $1000\rho^2(E0) = 154.4$ for the $0_2^+ \rightarrow 0_1^+$ transition. These comparisons are puzzling. On the one hand, the experimental 0_2^+ level is usually interpreted as having a dominant pair excitation character [54], while the 0_4^+ level would be the head of a β vibration [54].

To shed additional light on $E0$ transitions in ^{166}Er , the QRPA calculations provide the following information on 0^+ excitation energies and $\rho^2(E0; 0_i^+ \rightarrow 0_1^+)$ values, with $i = 2, 3, \text{ and } 4$, namely

- (i) Calculated excitation energies: $E(0_2^+) = 1724$ keV, $E(0_3^+) = 1956$ keV, and $E(0_4^+) = 2068$ keV. These values are shifted by approximately 200 keV toward higher energies when compared to those measured: 1460, 1713, and 1934 keV, for the 0_2^+ , 0_3^+ , and 0_4^+ levels, respectively.
- (ii) Calculated $1000\rho^2(E0) = 3.15$ for the $0_2^+ \rightarrow 0_1^+$ transition. This value is much weaker than that obtained from the 5DCH calculations. $1000\rho^2(E0) = 3.15$ is a value in agreement with that quoted in the Kibedi and Spear compilation [28], $1000\rho^2(E0) = 2.2(8)$, and with the value $1000\rho^2(E0) = 5.3(23)$ deduced from new measurements [40].

For the $0_3^+ \rightarrow 0_1^+$ transition, we have obtained $1000\rho^2(E0; 0_3^+ \rightarrow 0_1^+) = 0.16$, a weak value consistent with the interpretation that 0_3^+ is a dominant pair excitation [54]. The calculated $E0$ strength for the $0_4^+ \rightarrow 0_1^+$ transition suggests a collective strength, with magnitude five times stronger than that for the $0_2^+ \rightarrow 0_1^+$ transition, namely $1000\rho^2(E0; 0_4^+ \rightarrow 0_1^+) = 15.0$. This magnitude is weaker than that measured [40].

While the structure of 0_2^+ and 0_3^+ excited states seems reasonably well understood, that of 0_4^+ is here matter of concern. The reason because the experimental energy $E(0_4^+) = 1934$ keV is high if this level were to be interpreted as a β vibration [54].

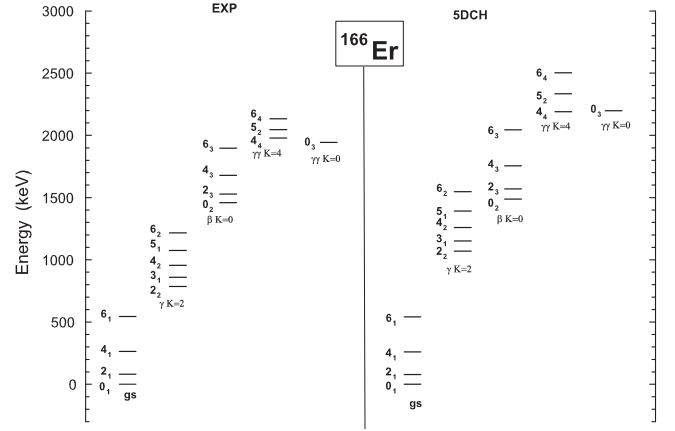


TABLE II. $B(E2)$ values in Weisskopf units (W.u.) for intraband transitions in ^{166}Er . Comparisons between experimental data and 5DCH calculations using the D1S force.

$I_i I_f$	Expt.	5DCH/D1S	$I_i I_f$	Expt.	5DCH/D1S
gs band \rightarrow gs band			γ band \rightarrow γ band		
$2_1^+ 0_1^+$	217 (5)	227.6	$3_1^+ 2_2^+$		398.9
$4_1^+ 2_1^+$	312 (11)	327.7	$4_2^+ 2_2^+$	138 (9)	134.8
$6_1^+ 4_1^+$	370 (20)	365.7	$4_2^+ 3_1^+$	370 (30)	297.0
$8_1^+ 6_1^+$	373 (14)	389.7	$5_1^+ 3_1^+$	300 (40)	218.0
			$5_1^+ 4_2^+$	310 (40)	212.7
			$6_2^+ 4_2^+$	225 (16)	270.2
β band \rightarrow β band					
$2_3^+ 0_2^+$		252.4			
$4_3^+ 2_3^+$		365.3			
$6_3^+ 4_3^+$		410.8			

The potential energy surface calculated for ^{166}Er as a function of the β_{20} and β_{40} deformations is shown in Fig. 15. This surface is obtained from constrained Hartree-Fock-Bogoliubov calculations similar to those adopted in [55]. Details of calculations are given in Appendix. As can be seen on the figure, this surface displays smooth variations against β_{20} and β_{40} . Finally, the potential minimum takes place at deformations $(\beta_{20}, \beta_{40}) = (0.35, 0.06)$.

The next step in the modeling would be solving a two-dimensional collective Hamiltonian, followed by calculation of $E0$ transitions strengths. Such a study is out of the scope of present work.

VIII. SUMMARY AND CONCLUSION

A comprehensive study of $E0$ transitions in nuclei was done. It relied upon extensive microscopic model calculations devoted to even-even nuclei spanning a broad mass region with $A > 30$. Many experimental data for $\rho^2(E0)$ strengths and $X(E0/E2)$ dimensionless parameters served as test cases, mainly to challenge the predictive power of the 5DCH theory implemented with the Gogny force, and to identify weakness in predictions. Several calculations conducted using the QRPA theory were also performed as complementary tests for the ^{166}Er and ^{238}U . isotopes. Our study offers the opportunity to test performance of the Church and Weneser $E0$

TABLE III. $B(E2)$ values in Weisskopf units (W.u.) for interband transitions in ^{166}Er . Comparisons between experimental data and 5DCH calculations using the D1S force.

$I_i I_f$	Expt.	5DCH/D1S	$I_i I_f$	Expt.	5DCH/D1S
γ band \rightarrow gs band			β band \rightarrow gs band		
$2_2^+ 0_1^+$	5.17 (21)	6.8			
$2_3^+ 2_1^+$	9.6 (6)	12.1			
$2_2^+ 4_1^+$	0.78 (4)	0.8			
$3_1^+ 2_1^+$		12.2	$0_2^+ 2_1^+$		17.0
$3_1^+ 4_1^+$	11.1 (7)	7.5	$2_3^+ 0_1^+$	2.7 (10)	2.8
$4_2^+ 2_1^+$	1.98 (12)	2.9	$2_3^+ 2_1^+$	0.66 (8)	4.3
$4_2^+ 4_1^+$	11.1 (7)	15.0	$2_3^+ 4_1^+$		9.8
$4_2^+ 6_1^+$	2.01 (14)	2.0	$4_3^+ 2_1^+$		3.5
$5_1^+ 4_1^+$	8.9 (11)	9.4	$4_3^+ 4_1^+$		3.7
$5_1^+ 6_1^+$	12.4 (15)	10.5	$4_3^+ 6_1^+$		9.6
$6_2^+ 4_1^+$	0.88 (6)	1.6			
$6_2^+ 6_1^+$	9.9 (7)	15.7			
β band \rightarrow γ band			$\gamma\gamma_{K=4}$ band \rightarrow γ band		
$0_2^+ 2_2^+$		0.12			
$2_3^+ 3_1^+$		0.04	$4_4^+ 2_2^+$	8 (3)	18.1
$2_3^+ 4_2^+$		0.17			
$4_3^+ 2_2^+$		0.02			
$4_3^+ 3_1^+$		0.13	$\gamma\gamma_{K=0}$ band \rightarrow γ band		
$4_3^+ 4_2^+$		0.04			
$4_3^+ 5_1^+$		0.10	$0_3^+ 2_2^+$	21 (6)	36.0
$4_3^+ 6_2^+$		0.18			

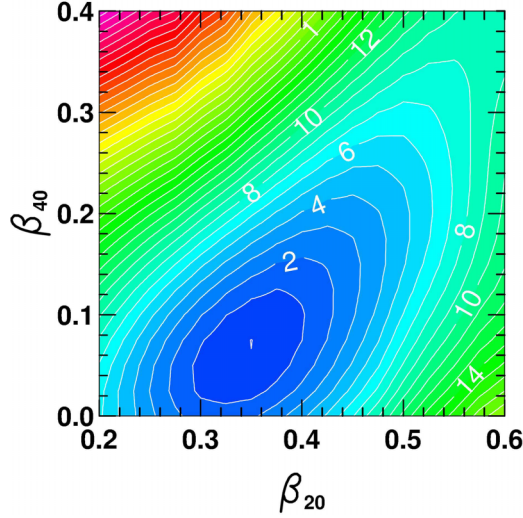


FIG. 15. ^{166}Er Potential energy surface (MeV) as a function of β_{20} and β_{40} deformations. The white isolines on the surface are separated by 1 MeV.

transition operator. To our knowledge, this is the first time that such an operator has been adopted in nuclear structure calculations.

In order to cure the predictions for $\rho^2(E0)$ values that were systematically found to be too strong in a previous publication [9], sensitivity calculations have shown that collective masses stronger than those based on the Inglis-Beliaev approximation lead to weaker strength of $\rho^2(E0)$ predictions. Such renormalized masses are based on phenomenological recipes and symmetry properties inherent to the 5DCH Hamiltonian. They considerably help lower the magnitude of the $\rho^2(E0)$ predictions, as does the Church and Weneser $E0$ transition operator. It is evident that stronger collective masses need be built based on theory. The QRPA approach may be a way to proceed, since this theory leads to collective masses at the minimum of potential energy that are approximately 30% stronger than Inglis-Beliaev masses [56]. The local quasiparticle QRPA (LQRPA) method would also be an asset to calculate collective masses at triaxial deformations. See for example, Ref. [57]. Finally, we have tested that the D1M force does not help reduce the strength of $E0$ transitions. This is the main reason why the D1S force was adopted throughout present study.

In general, $\rho^2(E0; 0_2^+ \rightarrow 0_1^+)$ predictions are in good agreement with patterns displayed by data along isotopic and isotonic chains. The present D1S calculations support in a satisfactory way the well known picture of phase transition predicted for the Zr isotopic chain in the vicinity of neutron number $N = 60$. A similar conclusion holds for the Nd, Sm, and Gd isotopes near $N = 90$.

Weakness in 5DCH model predictions is seen in many instances where experimental $X(E0/E2)$ values abruptly drop from strong to weak values. This feature is observed in the rare-earth region, that is in the vicinity of $N = 96$ among the Dy and Er isotopes. Strong mismatch is also observed between $1000\rho^2(E0)$ data and calculated values available for

a nucleus. As an illustration, see Fig. 9(f). The $E0$ transition operator cannot be blamed for such features.

Instead, we suspect that the 5DCH theory is not appropriate in these particular instances. A plausible strategy to make improvements in predictions would be to enrich the energy density functional by implementing 2qp components, and to use the generator coordinate method (GCM). Such a theory has been implemented and tested with success for interpreting $E0$ transitions in the Er isotopes [58]. It is the extended functional which operates in such a way that the eigenstates possess complex structures, which evolve from collective to quasiparticle character along the isotopic chain. This extended GCM theory has been implemented using the pairing plus quadrupole (PPQ) model [59] and the standard $E0$ transition operator [58]. If the Church and Weneser $E0$ operator were to be implemented in the theory instead, the proton and neutron effective charges would have to be modified. As an additional comment, we suggest the above extended GCM theory as the best approach adopt in systematic analyses of $E0$ transition strengths over the Segrè chart. Such a tremendous task would be made manageable by running calculations on exaflop computers of the next generation. Of course, the hope would be that the Gogny energy density functional would be implemented in such extended GCM studies.

APPENDIX: ^{166}Er POTENTIAL ENERGY SURFACE

The variational principle is applied to minimize the energy functional

$$\delta \langle \phi_{(q)} | \hat{H} - \lambda_N \hat{N} - \lambda_Z \hat{Z} - \sum_{i,j} \lambda_{ij} \hat{Q}_{ij} | \phi_{(q)} \rangle = 0, \quad (\text{A1})$$

where \hat{Q}_{ij} is an external field operator aimed at constraining the nuclear mean field to adopt a deformed shape, and λ_N , λ_Z , and λ_{ij} are Lagrange multipliers. Equation (A1) is solved for \hat{Q}_{20} and \hat{Q}_{40} , external fields generating axially symmetric quadrupole and hexadecapole deformations, respectively. The ket $|\phi_{(q)}\rangle$ is the quasiparticle vacuum state. \hat{H} , \hat{N} , and \hat{Z} are the nuclear Hamiltonian built using the D1S force and the neutron and proton numbers, respectively.

The constraints

$$\langle |\hat{N}| \rangle = N, \quad \langle |\hat{Z}| \rangle = Z, \quad \langle |\hat{Q}_{mn}| \rangle = q_{mn} \quad (\text{A2})$$

serve in the determination of the Lagrange multipliers.

The potential energy surface $V(q_{20}, q_{40})$ is calculated as

$$V(q_{20}, q_{40}) = \langle \phi_{(q)} | \hat{H} | \phi_{(q)} \rangle. \quad (\text{A3})$$

This surface is shown in Fig. 15 as a function of axial quadrupole and hexadecapole deformation parameters β_{20} and β_{40} , respectively. These deformation parameters are defined as

$$\beta_{20} = \sqrt{\frac{\pi}{5}} \frac{q_{20}}{A \langle r^2 \rangle}, \quad (\text{A4})$$

$$\beta_{40} = 3 \frac{q_{40}}{r_0^4 A^{\frac{7}{3}}} = \frac{27}{25} \frac{q_{40}}{A \langle r^2 \rangle^2}, \quad (\text{A5})$$

and

$$\langle r^2 \rangle = \frac{3}{5} (r_0 A^{\frac{1}{3}})^2 \quad \text{with } r_0 = 1.2 \text{ fm}. \quad (\text{A6})$$

- [1] A. Bohr and B. R. Mottelson, *Nuclear Structure* (Benjamin, Reading, MA, 1975)
- [2] P. E. Garrett, *J. Phys. G: Nucl. Part. Phys.* **27**, R1 (2001).
- [3] A. Arima and F. Iachello, *The Interacting Boson Model* (Cambridge University Press, Cambridge, 1987).
- [4] P. von Brentano, V. Werner, R. F. Casten, C. Scholl, E. A. McCutchan, R. Krucken, and J. Jolie, *Phys. Rev. Lett.* **93**, 152502 (2004).
- [5] J. L. Wood, E. F. Zganjar, C. De Coster, and K. Heyde, *Nucl. Phys. A* **651**, 323 (1999).
- [6] K. Heyde and J. L. Wood, *Rev. Mod. Phys.* **83**, 1467 (2011).
- [7] J. E. García-Ramos and K. Heyde, *Phys. Rev. C* **102**, 054333 (2020).
- [8] N. Gavrielov, A. Leviatan, and F. Iachello, *Phys. Rev. C* **105**, 014305 (2022).
- [9] J.-P. Delaroche, M. Girod, J. Libert, H. Goutte, S. Hilaire, S. Peru, N. Pillet, and G. F. Bertsch, *Phys. Rev. C* **81**, 014303 (2010).
- [10] M. Matsuzaki and T. Ueno, *Prog. Theor. Exp. Phys.* **2016**, 043D03 (2016).
- [11] G. Bertsch, *Eur. Phys. J. A* **55**, 248 (2019).
- [12] J. Libert, J.-P. Delaroche, M. Girod, H. Goutte, S. Hilaire, S. Peru, N. Pillet, and G. F. Bertsch, *J. Phys.: Conf. Ser.* **205**, 012007 (2010).
- [13] K. Kumar and M. Baranger, *Nucl. Phys. A* **92**, 608 (1967).
- [14] E. L. Church and J. Wenner, *Phys. Rev.* **103**, 1035 (1956).
- [15] J. F. Berger, M. Girod, and D. Gogny, *Comput. Phys. Commun.* **63**, 365 (1991).
- [16] S. Goriely, S. H. Hilaire, M. Girod, and S. Peru, *Phys. Rev. Lett.* **102**, 242501 (2009).
- [17] J. Libert, M. Girod, and J.-P. Delaroche, *Phys. Rev. C* **60**, 054301 (1999).
- [18] D. R. Inglis, *Phys. Rev.* **103**, 1786 (1956).
- [19] S. T. Beliaev, *Nucl. Phys.* **24**, 322 (1961).
- [20] M. Girod, J.-P. Delaroche, J.-F. Berger, and J. Libert, *Phys. Lett. B* **325**, 1 (1994).
- [21] D. J. Thouless and J. G. Valatin, *Nucl. Phys.* **31**, 211 (1962).
- [22] M. Girod, J.-P. Delaroche, A. Gorgen, and A. Obertelli, *Phys. Lett. B* **676**, 39 (2009).
- [23] J. O. Rasmussen, *Nucl. Phys.* **19**, 85 (1960).
- [24] J. Dechargé and D. Gogny, *Phys. Rev. C* **21**, 1568 (1980).
- [25] Brookhaven database, <http://www.nndc.bnl.gov/>.
- [26] R. D. O. Llewellyn, M. A. Bentley, R. Wadsworth, H. Iwasaki, J. Dobaczewski, G. de Angelis, J. Ash, D. Bazin, P. C. Bender, B. Cederwall, B. P. Crider, M. Doncel, R. Elder, B. Elman, A. Gade, M. Grindler, T. Haylett, D. G. Jenkins, I. Y. Lee, B. Longfellow, E. Lunderberg, T. Mijatovic, S. A. Milne, D. Muir, A. Pastore, D. Rhodes, and D. Weisshaar, *Phys. Rev. Lett.* **124**, 152501 (2020).
- [27] L. Gaudefroy, A. Obertelli, S. Peru, N. Pillet, S. Hilaire, J.-P. Delaroche, M. Girod, and J. Libert, *Phys. Rev. C* **80**, 064313 (2009).
- [28] T. Kibedi, A. B. Gamsworthy, and J. L. Wood, *Prog. Part. Nucl. Phys.* **123**, 103930 (2022), and references therein.
- [29] A. Turturică, C. Costache, P. Petkov, J.-P. Delaroche, M. Girod, J. Libert, G. Cata-Danil, S. Pascu, C. Mihai, M. Boromiza, D. Bucurescu, C. Clisu, D. Filipescu, N. M. Florea, I. Gheorghe, A. Ionescu, R. Lica, N. M. Marginean, R. Marginean, R. E. Mihai, A. Mitu, A. Negret, C. R. Nita, A. Olacel, A. Oprea, T. Sava, C. Sotty, L. Stan, I. Stiru, R. Suvaila, S. Toma, G. V. Turturica, and S. Ujenuic, *Phys. Rev. C* **103**, 044306 (2021).
- [30] Z. Gacsi, M. Csatos, A. Krasznahorkay, D. Sohler, J. Gulyas, J. Timar, M. Hunyadi, J. L. Weil, and J. van Klinken, *Phys. Rev. C* **64**, 047303 (2001).
- [31] T. R. Rodríguez, *Phys. Rev. C* **90**, 034306 (2014).
- [32] M. Siciliano, J. J. Valiente-Dobon, A. Goasduff, T. R. Rodriguez, D. Bazzacco, G. Benzoni, T. Braunroth, N. Cieplicka-Orynczak, E. Clement, F. C. L. Crespi, G. de France, M. Doncel, S. Erturk, C. Fransen, A. Gadea, G. Georgiev, A. Goldkuhle, U. Jakobsson, G. Jaworski, P. R. John, I. Kuti, A. Lemasson, H. Li, A. Lopez-Martens, T. Marchi, D. Mengoni, C. Michelagnoli, T. Mijatovic, C. Muller-Gatermann, D. R. Napoli, J. Nyberg, M. Palacz, R. M. Perez-Vidal, B. Saygi, D. Sohler, S. Szilner, and D. Testov, *Phys. Rev. C* **104**, 034320 (2021).
- [33] J.-P. Delaroche, M. Girod, and J. Libert (unpublished).
- [34] G. Wenes, P. Van Isacker, M. Waroquier, K. Heyde, and J. Van Maldeghem, *Phys. Rev. C* **23**, 2291 (1981).
- [35] F. Iachello, *Phys. Rev. Lett.* **85**, 3580 (2000).
- [36] F. Iachello, *Phys. Rev. Lett.* **87**, 052502 (2001).
- [37] Z. P. Li, T. Niksic, D. Vretenar, J. Meng, G. A. Lalazissis, and P. Ring, *Phys. Rev. C* **79**, 054301 (2009).
- [38] R. F. Casten and N. V. Zamfir, *Phys. Rev. Lett.* **87**, 052503 (2001).
- [39] D. A. Meyer, V. Wood, R. F. Casten, C. R. Fitzpatrick, G. Graw, D. Bucurescu, J. Jolie, P. von Brentano, R. Hertenberger, H.-F. Wirth, N. Braun, T. Faestermann, S. Heinze, J. L. Jerke, R. Krucken, M. Mahgoub, O. Moller, D. Mucher, and C. Scholl, *Phys. Rev. C* **74**, 044309 (2006).
- [40] K. Wimmer, R. Krucken, V. Bildstein, K. Eppinger, R. Gernhauser, D. Habs, C. Hinke, T. Kroll, R. Lutter, H.-J. Maier, P. Maierbeck, T. Morgan, O. Schaile, W. Schwerdtfeger, S. Schwertel, and P. G. Thirolf, *AIP Conf. Proc.* **1090**, 539 (2009).
- [41] A. Chakraborty, E. E. Peters, B. P. Crider, C. Andreoiu, P. C. Bender, D. S. Cross, G. A. Demand, A. B. Gamsworthy, P. E. Garrett, G. Hackman, B. Hadinia, S. Ketelhut, Ajay Kumar, K. G. Leach, M. T. McEllistrem, J. Pore, F. M. Prados-Estevez, E. T. Rand, B. Singh, E. R. Tardiff, Z.-M. Wang, J. L. Wood, and S. W. Yates, *Phys. Rev. Lett.* **110**, 022504 (2013).
- [42] F. M. Prados-Estevez, E. E. Peters, A. Chakraborty, M. G. Mynk, D. Bandyopadhyay, N. Boukharouba, S. N. Choudry, B. P. Crider, P. E. Garrett, S. F. Hicks, A. Kumar, S. R. Leshner, C. J. McKay, M. T. McEllistrem, S. Mukhopadhyay, J. N. Orce, M. Scheck, J. R. Vanhoy, J. L. Wood, and S. W. Yates, *Phys. Rev. C* **95**, 034328 (2017).
- [43] R. Krücken, B. Albanna, C. Bialik, R. F. Casten, J. R. Cooper, A. Dewald, N. V. Zamfir, C. J. Barton, C. W. Beausang, M. A. Caprio, A. A. Hecht, T. Klug, J. R. Novak, N. Pietralla, and P. von Brentano, *Phys. Rev. Lett.* **88**, 232501 (2002).
- [44] L. L. Riedinger, E. G. Funk, J. W. Mihelich, G. S. Schilling, A. E. Rainis, and R. N. Oehlberg, *Phys. Rev. C* **20**, 2170 (1979).
- [45] J. Wiederhold, R. Kern, C. Lizarazo, N. Pietralla, V. Werner, R. V. Jolos, D. Bucurescu, N. Florea, D. Ghita, T. Glodariu, R. Lica, N. Marginean, R. Marginean, C. Mihai, R. Mihai, I. O. Mitu, A. Negret, C. Nita, A. Olacel, S. Pascu, L. Stroe, S. Toma, and A. Turturica, *Phys. Rev. C* **94**, 044302 (2016).
- [46] M. Spieker, S. Pascu, D. Bucurescu, T. M. Shneidman, T. Faestermann, R. Hertenberger, H.-F. Wirth, N.-V. Zamfir, and A. Zilges, *Phys. Rev. C* **97**, 064319 (2018).
- [47] A. I. Levon, G. Graw, Y. Eisermann, R. Hertenberger, J. Jolie, N. Yu. Shirikova, A. E. Stuchbery, A. V. Sushkov, P. G. Thirolf, H.-F. Wirth, and N. V. Zamfir, *Phys. Rev. C* **79**, 014318 (2009).

- [48] A. I. Levon, G. Graw, R. Hertenberger, S. Pascu, P. G. Thirolf, and H.-F. Wirth, and P. Alexa, *Phys. Rev. C* **88**, 014310 (2013).
- [49] J.-W. Cui, X.-R. Zhou, F.-Q. Chen, Y. Sun, C.-L. Wu, and Z.-C. Gao, *Phys. Rev. C* **90**, 014321 (2014).
- [50] S. Goriely, S. Hilaire, S. Peru, and K. Sieja, *Phys. Rev. C* **98**, 014327 (2018).
- [51] M. Dupuis, G. Haouat, J.-P. Delaroche, E. Bauge, and J. Lachkar, *Phys. Rev. C* **100**, 044607 (2019).
- [52] S. Peru, G. Gosselin, M. Martini, M. Dupuis, S. Hilaire, and J.-C. Devaux, *Phys. Rev. C* **83**, 014314 (2011).
- [53] J. T. H. Dowie, T. Kibedi, T. K. Eriksen, and A. E. Stuchbery, *At. Data Nucl. Data Tables* **131**, 101283 (2020).
- [54] P. E. Garrett, M. Kadi, C. A. McGrath, V. Sorokin, M. Li, M. Yeh, and S. W. Yates, *Phys. Lett. B* **400**, 250 (1997).
- [55] J.-P. Delaroche, M. Girod, H. Goutte, and J. Libert, *Nucl. Phys. A* **771**, 103 (2006).
- [56] F. Lechaftois, I. Deloncle, and S. Peru, *Phys. Rev. C* **92**, 034315 (2015).
- [57] N. Hinohara, K. Sato, T. Nakatsukasa, M. Matsuo, and K. Matsuyanagi, *Phys. Rev. C* **82**, 064313 (2010).
- [58] F.-Q. Chen and J. L. Egido, *Phys. Rev. C* **93**, 064313 (2016).
- [59] M. Baranger and K. Kumar, *Nucl. Phys. A* **122**, 241 (1968).